J. Fluid Mech. (2001), *vol.* 449, *pp.* 39–59.
DOI: 10.1017/S0022112001006097 Printed in the United Kingdom

Generation of collimated jets by a point source of heat and gravity

By VLADIMIR SHTERN AND FAZLE HUSSAIN

Department of Mechanical Engineering, University of Houston, Houston, TX 77204-4006, USA

(Received 10 August 2000 and in revised form 5 June 2001)

New solutions of the Boussinesq equations describe the onset of convection as well as the development of collimated bipolar jets near a point source of both heat and gravity. Stability, bifurcation, and asymptotic analyses of these solutions reveal details of jet formation. Convection (with l cells) evolves from the rest state at the Rayleigh number $Ra = Ra_{cr} = (l-1)l(l+1)(l+2)$. Bipolar ($l = 2$) flow emerges at $Ra = 24$ via a transcritical bifurcation: $Re = 7(24 - Ra)/(6 + 4Pr)$, where Re is a convection amplitude (dimensionless velocity on the symmetry axis) and Pr is the Prandtl number. This flow is unstable for small positive values of Re but becomes stable as Re exceeds some threshold value. The high-Re stable flow emerges from the rest state and returns to the rest state via hysteretic transitions with changing Ra. Stable convection attains high speeds for small Pr (typical of electrically conducting media, e.g. in cosmic jets). Convection saturates due to negative 'feedback': the flow mixes hot and cold fluids thus decreasing the buoyancy force that drives the flow. This 'feedback' weakens with decreasing Pr, resulting in the development of high-speed convection with a collimated jet on the axis. If swirl is imposed on the equatorial plane, the jet velocity decreases. With increasing swirl, the jet becomes annular and then develops flow reversal on the axis. Transforming the stability problem of this strongly non-parallel flow to ordinary differential equations, we find that the jet is stable and derive an amplitude equation governing the hysteretic transitions between steady states. The results obtained are discussed in the context of geophysical and astrophysical flows.

1. Introduction

This paper deals with a very simple buoyancy problem: thermal convection near a point source of heat and gravity. Despite its apparent simplicity, the problem is rich in interesting effects such as hysteresis, flow reversal, and collapse; the most intriguing among them is the development of highly collimated bipolar jets. We attempt here to explain these effects with the help of exact solutions of the Boussinesq equations. The spherical symmetry of the equilibrium state of rest and the conical similarity of the emerging buoyancy-driven flow allow us to obtain analytical solutions for (i) the linear stability problem of the rest state, (ii) the weakly nonlinear problem of flow bifurcation, and (iii) the strongly nonlinear problem of the formation of high-speed jets.

There is a practical relevance of this simple convection problem to geophysical and astrophysical situations, particularly in the formation of collimated cosmic jets. This relevance is discussed at the end of the paper.

Here, we present (i) a new stability approach for conically similar convection, (ii) a

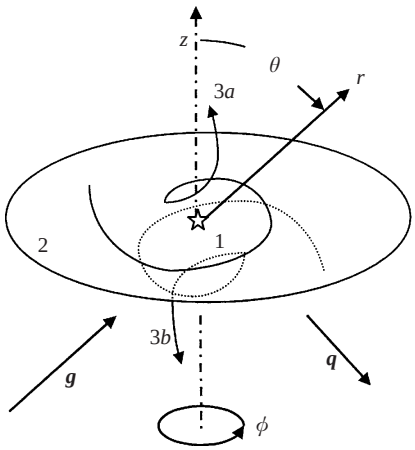

FIGURE 1. Schematic of the problem. The star 1 at the origin of spherical coordinates (r, θ, ϕ) denotes a point source of gravity $\boldsymbol{g}$ and heat flux $\boldsymbol{q}$, which, in the presence of swirl in the accretion disk 2, induces bipolar helical convection (curves $3a$ and $3b$).

new asymptotic technique for high-speed convection flows, and (iii) a new amplitude equation governing hysteretic transitions between steady states. Using these tools, we obtain analytical and numerical solutions that help explain the mechanism of jet formation, particularly the development of bipolar collimated jets.

Following the problem formulation in § 2, we study the formation of jets via instability and their bifurcation, hysteresis, and collimation in §§ 3–6. In § 3, we consider the linear instability of the equilibrium state of rest and find critical values of Rayleigh numbers Ra and neutral modes. Using a weakly nonlinear expansion, we show in § 4 that the bipolar neutral mode transforms into finite-amplitude steady convection via a transcritical bifurcation. The results for finite-amplitude convection have been obtained numerically using the procedure described in § 5.1. These results reveal the hysteretic nature of the appearance and disappearance of stable convection (§ 5). We show in § 6 that this stable convection develops into a high-speed collimated jet for small Prandtl number Pr (relevant to cosmic jets) and find asymptotic solutions for this jet. In § 7, we consider swirl imposed in the equatorial plane (modelling the accretion disk in cosmic flows) and show that with increasing swirl, the jet becomes annular, and then flow reversal occurs on the axis. Finally, in § 8, we study the stability of the convective flows, show that the jet is stable, and derive an amplitude equation governing the hysteretic transitions between steady states. In § 9, we summarize the results and discuss features of these buoyancy-driven jets in the context of geophysical and astrophysical flows.

2. Problem formulation

The problem is schematically represented in figure 1. At the origin of the spherical coordinates (r, θ, ϕ), we place a point source (PS, marked by a star symbol) of both heat flux, $\boldsymbol{q} = \gamma k r^{-2} \boldsymbol{e}_r$, and gravitational acceleration, $\boldsymbol{g} = -\delta r^{-2} \boldsymbol{e}_r$. Dimensional constants γ and δ characterize the strength of $\boldsymbol{q}$ and $\boldsymbol{g}$: $\gamma = Q/4(\pi k)$, where Q is the heat flux through a surface enclosing PS and δ is the PS mass multiplied by the gravitational constant; $\boldsymbol{e}_r$ is the radial unit vector, and k is the thermal conductivity. The ambient medium is a viscous fluid whose self-gravitation is neglected.

We impose symmetry and impermeability conditions on the $\theta = 90^\circ$ (equatorial) plane 2 in figure 1 (modelling the accretion disk, see §9). On this plane, we consider three different boundary conditions for velocity: (i) stress-free, (ii) no-slip, and (iii) potential-vortex motion. For conditions (i) and (ii), an equilibrium state of rest exists. Conservation of Q yields that the temperature field of the rest state is $T = T_\infty + \gamma/r$. Since the temperature is infinite at $r = 0$, this model is the far-field approximation where the distance from the central body is much larger than the radius of the body (typical of point-source problems).

We apply the Boussinesq approximation, $\rho/\rho_\infty = 1 - \beta(T - T_\infty)$, where β is the coefficient of thermal expansion. Then, the buoyancy force is $\boldsymbol{F}_E = \rho_\infty \nu^2 r^{-3} G \boldsymbol{e}_r$ which is balanced by the radial gradient of pressure. Here $G = \beta\gamma\delta/\nu^2$ is the Grashof number, ν is the kinematic viscosity, and subscript E denotes the equilibrium state.

Now, we introduce a dimensionless temperature perturbation, ϑ, such that the total temperature field is given by

$$T = T_\infty + (1 + Pr\vartheta)\gamma/r, \tag{1}$$

where $Pr(\equiv \nu/\kappa)$ is the Prandtl number and κ is the thermal diffusivity. Then, the perturbed part of the buoyancy force (which may induce thermal convection) is $\boldsymbol{F}_C = \rho_\infty \nu^2 r^{-3} Ra\vartheta \boldsymbol{e}_r$; here $Ra \equiv PrG$ is the Rayleigh number, and subscript C denotes convection.

Since $\boldsymbol{g}$ and $\boldsymbol{q}$ have opposite directions, the thermal stratification is unstable when Ra exceeds a critical value, and convection develops. Due to the presence of the disk, the convection is bipolar, e.g. curves 3*a* and 3*b* in figure 1 depict streamlines of the helical flow converging near the swirling disk and going away from the source along the rotation axis z. The flow does not disturb the temperature field if $Pr = 0$; this is a reason to put Pr before ϑ in (1).

To summarize, we study flows governed by the Boussinesq equations,

$$\left.\begin{aligned} \partial \boldsymbol{v}/\partial t + (\boldsymbol{v}\cdot\nabla)\boldsymbol{v} &= \nu\Delta\boldsymbol{v} + (\boldsymbol{F}_C - \nabla p)/\rho_\infty, \quad \nabla\cdot\boldsymbol{v} = 0, \\ \partial T/\partial t + (\boldsymbol{v}\cdot\nabla)T &= \kappa\Delta T, \end{aligned}\right\} \tag{2}$$

where $\boldsymbol{v} = \{v_r, v_\theta, v_\phi\}$ is the velocity, p is the perturbed pressure, and t is the time. To find how these flows evolve, we start with the linear instability of the rest state where $\boldsymbol{v} = 0$.

3. Instability of the rest state

3.1. *Critical values of the Rayleigh number*

First, consider the onset of convection in the absence of the disk. In this case, the spherical symmetry of the problem permits representation of the infinitesimal temperature disturbances in the form

$$\vartheta = Cf(r)Y_l^m(x, \phi)\exp(\lambda t). \tag{3}$$

Here C is a constant, f is the unknown radial distribution, Y_l^m are the spherical harmonics, l and m are integers corresponding to the wavenumbers in the polar (θ) and azimuthal (ϕ) directions (figure 1), $x = \cos\theta$, and λ (which is real in this case) is the temporal growth rate. The velocity and pressure disturbances have similar representations. Then, equations (2) reduce to a single ordinary differential equation (ODE) for $f(r)$ (Chandrasekhar 1981, p. 223). To find critical values of Ra, we consider

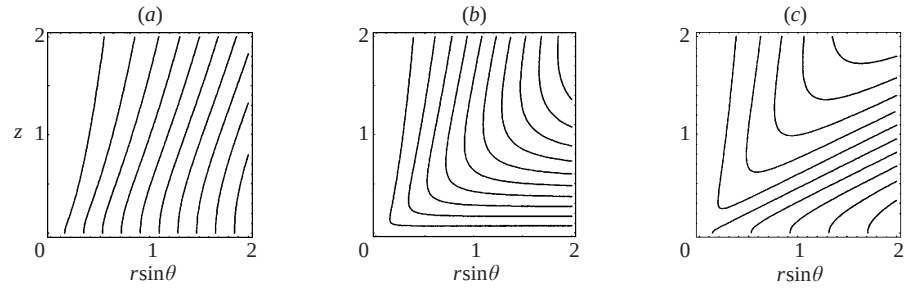

FIGURE 2. Streamlines of axisymmetric convection, in the absence of the accretion disk, for neutral modes with polar-angle wavenumber l: (*a*) $l = 1$, (*b*) $l = 2$, and (*c*) $l = 3$.

disturbances with $\lambda = 0$. This ODE can then be written as

$$\mathscr{D}_l^2[A(r)\,\mathscr{D}_l(r^{-1}f)] + l(l+1)Ra[rB(r)]^{-1}f = 0, \tag{4}$$

where $\mathscr{D}_l = [\mathrm{d}/\mathrm{d}r(r^2\mathrm{d}/\mathrm{d}r) - l(l+1)]/r^2$. Functions $A(r)$ and $B(r)$ depend on the radial distribution of gravity and the equilibrium temperature. In our case where $A(r) = B(r) = r^3$ (because $\boldsymbol{g} \sim r^{-2}$ and $T - T_\infty \sim r^{-1}$), equation (4) admits power-law solutions: $f(r) = r^\alpha$ and we find the analytical relation between Ra and α

$$Ra = (\alpha^2 - l^2)(1 - l - \alpha)(\alpha - l - 2)[\alpha^2 - (l+1)^2]/(l + l^2), \quad l = 1, 2, \ldots\ . \tag{5a}$$

For neutral modes, the power-law dependence on r of the temperature disturbances must be the same as that for the equilibrium temperature. Examining (1), we see that ϑ must be r-independent, i.e. $\alpha = 0$. Then (5*a*) gives the critical values of the Rayleigh number Ra_{cr} in the compact form.

$$Ra_{cr} = (l-1)l(l+1)(l+2), \quad l = 1, 2, \ldots\ . \tag{5b}$$

To find the convection patterns emerging at Ra_{cr}, we consider the neutral modes in more detail.

3.2. *Convection patterns*

We start with $l = 1$ which corresponds to $Ra_{cr} = 0$ according to (5*b*). The axisymmetric ($m = 0$) neutral mode is

$$\vartheta = x/2, \quad \{v_r, v_\theta \sin\theta, v_\phi\} = vr^{-1}\{x, (x^2-1)/2, 0\}. \tag{6a}$$

We have taken $C = 1/2$ in (3) to normalize (6*a*) such that $rv_r/v = 1$ on the positive z-axis, $x = 1$. Then, the Reynolds number $Re \equiv rv_r(1)/v$ serves as a convection amplitude. (Note that (6*a*) coincides with the (small-Re) solutions obtained by Landau 1944 and Rumer 1952.)

The neutral mode (6*a*) corresponds to the flow shown in figure 2 (*a*) (we depict only one quadrant of the meridional plane, $\phi = \text{const}$, since the streamline patterns are symmetric with respect to both the abscissa and the ordinate). Being unidirectional, this flow does not satisfy the condition of zero normal velocity on the plane $z = 0$ in figure 1, so this solution is inappropriate for the problem with an impermeable disk.

For $m = \pm 1$, we obtain three-dimensional neutral disturbances of the form

$$\vartheta = \tfrac{1}{2}(1 - x^2)^{1/2}\cos\phi, \quad \{v_r, v_\theta \sin\theta\} = vr^{-1}\{2\vartheta, x\vartheta\}, \quad v_\phi \sin\theta = vr^{-1}\vartheta\tan\phi. \tag{6b}$$

This flow is the same as that described by (6*a*) but in the coordinate frame rotated by 90° in the θ-direction.

Seeking a solution relevant for the disk problem, we consider the next value, $l = 2$, which corresponds to $Ra_{cr} = 24$ according to (5*b*).

Now the axisymmetric ($m = 0$) neutral mode is

$$\vartheta = x^2/4 - 1/12, \quad \{v_r, v_\theta \sin\theta, v_\phi\} = vr^{-1}\{(3x^2-1)/2, (x^3-x)/2, 0\}. \tag{7a}$$

The integration constant, $-1/12$, for ϑ is chosen to reduce the disturbance heat flux to zero: $\int_{-1}^{1} \vartheta \, dx = 0$. Solution (7*a*) satisfies the impermeability condition, $v_\theta = 0$ at $x = 0$ (see figure 2*b*) and is therefore relevant for the disk problem.

There are three-dimensional neutral disturbances with $m = \pm 2$:

$$\vartheta = \tfrac{1}{2}(1-x^2)^{1/2}\cos(2\phi), \quad \{v_r, v_\theta \sin\theta\} = vr^{-1}\{2\vartheta, x\vartheta\}, \quad v_\phi \sin\theta = vr^{-1}\vartheta\tan(2\phi). \tag{7b}$$

For any $l > 2$, there are (i) an axisymmetric neutral mode with $v_r \sim vr^{-1}P_l(x)$, where $P_l(x)$ is the Legendre polynomial, and (ii) three-dimensional neutral modes with $m = \pm l$ and $v_r \sim vr^{-1}(1-x^2)^{1/2}\cos(l\phi)$. As an example, the flow pattern for the $l = 3$ axisymmetric solution is shown in figure 2(*c*). Note that l is the number of convection cells for axisymmetric flows. The impermeability condition on the disk permits only even values of l.

Now that we have investigated the neutral modes of the rest state, we examine in the next section the nonlinear effects in the vicinity of $Ra = Ra_{cr}$ and, in particular, the bifurcation character (supercritical, subcritical, or transcritical) for the $l = 2$ axisymmetric mode.

4. Weakly nonlinear analysis of convection onset

4.1. *Weakly nonlinear approach*

Since the problem has no length scale, the convection is self-similar. The linear stability results (§ 3.2) show that this similarity is conical. Therefore, for steady axisymmetric convection, the temperature and velocity fields may be represented as

$$\left.\begin{aligned} T = T_\infty + \gamma r^{-1}(1 + Pr\vartheta), \quad \Psi = vr\psi, \\ v_r = -vr^{-1}\psi', \quad v_\theta = -v(r\sin\theta)^{-1}\psi, \quad v_\phi = 0. \end{aligned}\right\} \tag{8}$$

Here, Ψ is the Stokes stream function, ϑ and ψ (the dimensionless stream function) depend only on x, and the prime denotes differentiation with respect to x. Substituting (8) in (2), with some simple transformations, we obtain the ODEs

$$(1-x^2)\psi^{\mathrm{iv}} - 4x\psi''' - (\psi^2/2)''' = Ra\psi(1 + Pr\vartheta)/(1-x^2), \tag{9a}$$

$$(1-x^2)\vartheta' = \psi(1 + Pr\vartheta). \tag{9b}$$

We impose the conditions that the velocity must be bounded on the symmetry axis, $x = \pm 1$,

$$\psi(\pm 1) = 0, \quad |\psi'(\pm 1)| < \infty. \tag{10a}$$

Further, the temperature disturbances must not change the global heat flux; this yields the integral condition

$$\int_{-1}^{1} \vartheta(1 - Pr\psi') \, dx = 0. \tag{10b}$$

For ease of analysis, it is convenient to introduce an auxiliary function F whose third derivative equals the right-hand side of (9a), i.e.

$$F''' = Ra\psi(1 + Pr\vartheta)/(1 - x^2). \tag{11a}$$

Then, equation (9a) is integrated three times to yield

$$(1 - x^2)\psi' + 2x\psi - \tfrac{1}{2}\psi^2 = F. \tag{11b}$$

To find the boundary conditions for F, we differentiate (11b), and use (10a) to obtain $F'(\pm 1) = 0$. This new condition replaces that for ψ' in (10a):

$$\psi(\pm 1) = F'(\pm 1) = 0. \tag{11c}$$

The condition $\psi(\pm 1) = 0$ indicates that there is no fluid source on the z-axis, i.e. at $x = \pm 1$. To physically interpret the condition $F'(\pm 1) = 0$, we calculate the tangential stress $\tau_{r\theta} = \rho\nu[r^{-1}\partial v_r/\partial\theta + r\partial/\partial r(v_\theta/r)]$ in terms of F'. Using (8) and the derivative of (11b), we find that $\tau_{r\theta} = -F'\rho\nu^2(r^2 \sin\theta)^{-1}$. Thus, $F'(\pm 1) = 0$ indicates that $\tau_{r\theta}$ is bounded on the axis.

Finally, (11b) and (10a) yield

$$F(\pm 1) = 0. \tag{11d}$$

The problem (9b), (10b) and (11a–d) has the trivial solution $\psi = \vartheta = 0$, which corresponds to the rest state. However, at a critical value of $Ra = Ra_{cr}$, a non-trivial solution arises representing the onset of convection. To find analytical solutions for convection of a small but finite amplitude, we apply the power-law expansion near $Ra = Ra_{cr}$,

$$\psi = Re\psi_1 + Re^2\psi_2 + \ldots, \quad \vartheta = Re\vartheta_1 + Re^2\vartheta_2 + \ldots, \quad Ra = Ra_{cr} + ReRa_1 + Re^2Ra_2 + \ldots . \tag{12}$$

Here the Reynolds number, $Re \equiv rv_r(1)/\nu$ (the dimensionless velocity on the positive z-axis), serves as the small parameter. In (12), $\psi_1 (= -v_\theta r \sin\theta/\nu)$ and ϑ_1 are linear solutions obtained in § 3.2, e.g. (7a). Therefore, we do not need to solve the $O(Re)$ equations (which follow from (9) by omitting the nonlinear terms). Using (12) and (9), we obtain the $O(Re^2)$ equations,

$$(1-x^2)\psi_2^{\mathrm{iv}} - 4x\psi_2''' - Ra_{cr}\psi_2/(1-x^2) = (\psi_1^2/2)''' + (Ra_1 + Ra_{cr}Pr\vartheta_1)\psi_1/(1-x^2), \tag{13a}$$

$$(1 - x^2)\vartheta_2' - \psi_2 = Pr\psi_1\vartheta_1. \tag{13b}$$

Note that while ψ_1 and ϑ_1 are known, Ra_1 still has to be determined. Since substituting $\psi_2 = \psi_1$ makes the left-hand side of (13a) zero, equation (13a) is solvable only if its right-hand side is orthogonal to the solution w of the adjoint problem. Since the left-hand-side operator of (13a) is self-adjoint, we have $w = \psi_1$. Multiplying (13a) by ψ_1 and integrating from $x = -1$ to $x = 1$, we reduce the left-hand side to zero and find Ra_1. Since the coefficient multiplying Ra_1 is not zero (being positive), Ra_1 is uniquely determined (as well as Ra_j for $j > 1$). Now ψ_2 and ϑ_2 are determined by solving (13). Higher-order coefficients in (12) are obtained using a similar technique. As the smallest Ra_{cr} is physically important, we now consider in more detail only the $l = 2$ case for the symmetry condition on the disk (figure 2b).

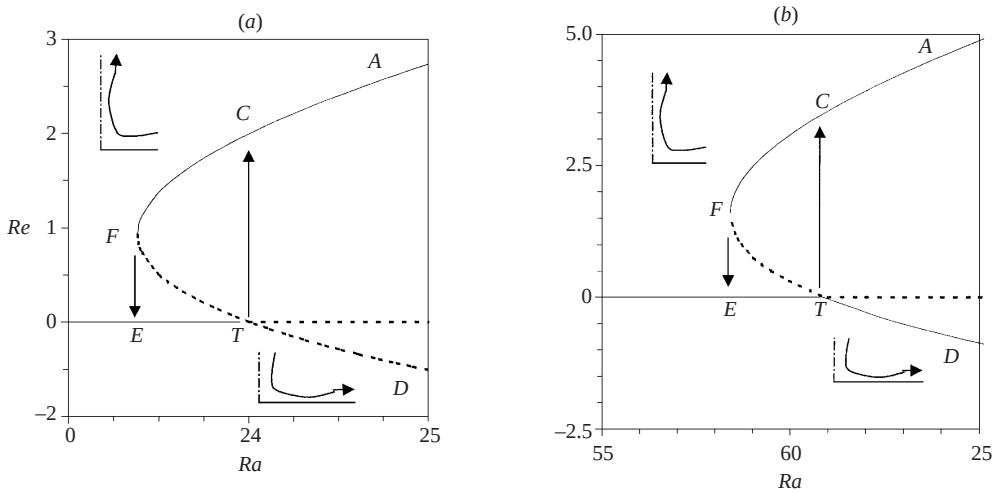

FIGURE 3. Velocity (Re) on the positive z-axis vs. Rayleigh number Ra at Prandtl number $Pr = 1$: (a) stress-free, (b) no-slip disk. The line $Re = 0$ represents the rest state, and curve $ACFTD$ represents convection with the $l = 2$ cells (insets, see also figure 2b). Solid and broken curves denote stable and unstable solutions, respectively.

4.2. *Bifurcation of bipolar convection*

The results of § 3.2 (i.e. (7a) and $Ra_{cr} = 24$) and the above expansion procedure yield

$$\left.\begin{aligned} &\psi_1 = x(1-x^2)/2, && \psi_2 = (5+Pr)x^3(1-x^2)/112, \\ &\vartheta_1 = x^2/4 - 1/12, && \vartheta_2 = [(5+15Pr)x^4 - 28Prx^2/3 - 1 + Pr/9]/448, \\ &Ra_1 = -(6+4Pr)/7, && Ra_2 = (560+57Pr+244Pr^2)/4704. \end{aligned}\right\} \quad (14)$$

Substituting (14) in (12), we note two important features:

(a) the bifurcation is transcritical (see the vicinity of point T in figure 3a), i.e. the secondary solution exists for both $Ra < Ra_{cr}$ (branch TF) and $Ra > Ra_{cr}$ (branch TD);

(b) the flow near the equatorial plane is converging for $Ra < Ra_{cr}$ and diverging for $Ra > Ra_{cr}$ (see the insets in figure 3a).

The general theory (Chossat 1979; Golubitsky & Schaeffer 1982) predicts that the secondary solution for $|Re| \ll 1$ is unstable with respect to axisymmetric disturbances for $Ra < Ra_{cr}$ and with respect to the $m = 2$ disturbances for $Ra > Ra_{cr}$ (broken curve FTD in figure 3a). However, as Re exceeds some threshold value, the flow may become stable. Using (14) and neglecting higher-order terms in (12), we observe that as Re increases, Ra first decreases, reaches its minimum, and then increases. In order to examine the flow away from the vicinity of the bifurcation point T, we use numerical analysis, which is discussed in the next section.

5. Development of bipolar convection via hysteresis

5.1. *Numerical procedure*

For the stress-free problem, we integrate (9b), (11a) and (11b) from $x = 1$ to $x = -1$, with initial conditions (11c,d) and guesses for $F''(1)$, $\vartheta(1)$ and $\psi'(1)$. (Resolving the 0/0-type indeterminacy gives $\vartheta'(1)$ from (9b) and $F'''(1)$ from (11a) but not $\psi'(1)$ from (11b).) To satisfy the three conditions (10b) and (11c) at $x = -1$, we adjust $F''(1)$,

$\vartheta(1)$, and $\psi'(1)$ using the Newton shooting method. Ra and Pr are free (i.e. control) parameters. In some instances, it is more convenient to use $Re = -\psi'(1)$ as a free parameter and to find Ra by the shooting method. Once a converged solution for given parameter values is obtained by the Newton method, we gradually increase the free parameter (e.g. Ra or Re) using the previous solution as an initial guess for the following shooting. For numerical integration, we use the fourth-order Runge–Kutta procedure and the Chebyshev grid with 200 steps. In order to check accuracy, we have also used 400 steps and verified that all digits shown here for the numerical results are correct.

5.2. *Finite-amplitude convection above a stress-free disk*

Figure 3(a) shows the numerical results for the stress-free case on the parameter plane (Ra, Re) at $Pr = 1$. The equilibrium (rest) state E corresponds to the $Re = 0$ line. At point T (separating the solid and broken parts of the $Re = 0$ line), transcritical bifurcation of the $l = 2$ convection occurs. Curve $ACFTD$ representing this convection has two branches, FCA and FTD, which meet at fold F where Ra reaches its minimum value $Ra_F = 23.37$ at $Re = Re_F = 0.922$. The solid and broken lines in figure 3(a) indicate stable and unstable solutions respectively. The equilibrium state is unstable for $Ra > 24$ as shown in § 3, and the steady flow is unstable near T (as discussed in § 4.2). Branch FCA is depicted by a solid line because the flow becomes stable for $Re > Re_F$ (see § 8). Infinitesimal disturbances cause switching between the rest state and the flow near points T and F (as shown by arrows FE and TC in figure 3). Thus, a hysteresis loop exists composed of the stable states and the transient trajectories – $ETCFE$ in figure 3.

5.3. *No-slip disk*

In this case, we integrate (9b), (11a) and (11b) from $x = 0$ to $x = 1$ with the initial conditions: $\psi(0) = F(0) = 0$ (no-slip), $F'(0) = 1$ (normalization used at $Re = 0$ only), and guessed values of $F''(0)$ and Ra. Since $x = 1$ is a singular point of the equations, an initial-value solution may be unbounded at $x = 1$. For this reason, the integration is terminated at $x = x_f < 1$ (say, $x_f = 0.9999$), and then all necessary quantities (in particular, ψ and F') are extrapolated to $x = 1$. To satisfy the condition $F'(1) = 0$, we adjust $F''(0)$ by shooting. Then, we find the values of Ra (i.e. Ra_{cr}) that make ψ zero at $x = 1$: $Ra_{cr} = 60.89$ for $l = 2$, $Ra_{cr} = 566.22$ for $l = 4$, and so on. Recall that l is the number of convection cells, and the presence of the disk allows only even l. Next, we obtain solutions for $Re \neq 0$ using the Newton shooting procedure.

Figure 3(b), shows the numerical results for steady convection above the no-slip disk at $Pr = 1$. An important difference with the stress-free disk (figure 3a) is that the descending flow (branch TD) is stable. (Note that neutral modes (7b) do not satisfy the no-slip condition and there is no growing three-dimensional disturbance near T in figure 3b.) Thus, there are two stable convection states: ascending (A) along branch FCA (see the upper inset in figure 3b) and descending (D) along branch TD (the lower inset). Branch FT corresponds to the unstable solutions.

A common feature for both the cases of stress-free and no-slip conditions on the disk is the development of stable ascending convection (branch FCA in figure 3) via a fold bifurcation (at point F). Thus, in both cases, the flow appears (as Ra increases) and disappears (as Ra decreases) via hysteretic transitions (arrows TC and FE). While the ascending flow (characterized here by Re) is moderate at $Pr = 1$ (figure 3), the flow becomes high speed (i.e. $Re \gg 1$) and a strong near-axis jet develops as the

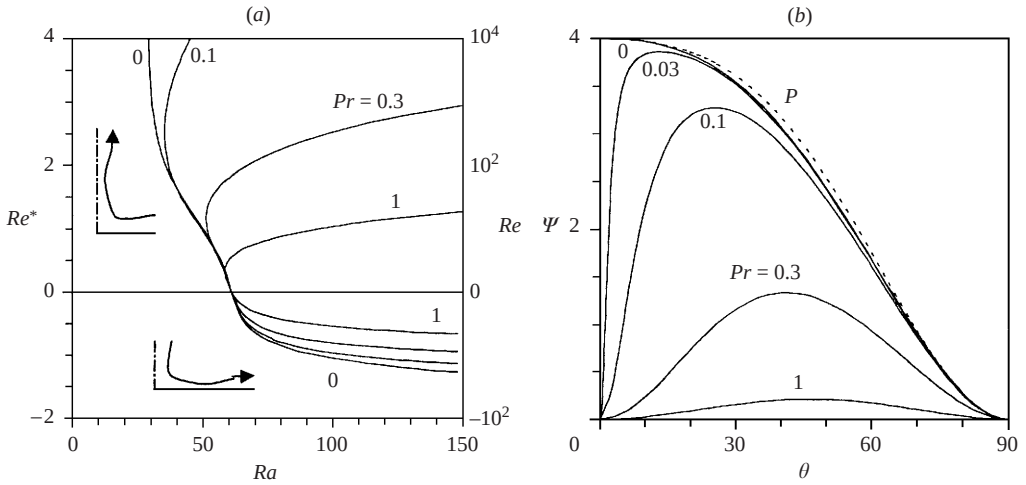

FIGURE 4. (*a*) Dependence of the flow above the no-slip disk on Prandtl number Pr; (*b*) profiles of the stream function ψ at the fold points in (*a*) (the $Pr = 0.03$ case being additional) showing the development of the near-axis boundary layer as $Pr \to 0$. Curve P depicts the polynomial approximation, $10x^2 - 6x^3$, of the $Pr = 0$ curve in (*b*).

Prandtl number tends to zero at a fixed Ra. The development and features of this jet are explained below with the help of asymptotic solutions for large Re.

6. Development of strong jets

6.1. *Role of the Prandtl number in the jet formation*

There is a clear physical reason for the development of strong jets when the Prandtl number Pr is small. While the linear instability of the rest state depends only on Ra, the nonlinear saturation of convection depends on Pr as well. The saturation results from negative 'feedback': convection mixes hot and cold fluids, i.e. reduces temperature gradients, thereby reducing the buoyancy force that drives the flow. The feedback strength depends on Pr: even weak mixing significantly changes the temperature field for large Pr (e.g. in silicon oils) while the temperature field is flow-independent at $Pr = 0$. (Note that in cosmic jets, heat transfer (which occurs by radiation) is nearly flow-independent; a small *effective* Prandtl number may be used to model this effect.) Thus, for small Pr, nonlinear saturation occurs only when convection becomes high speed.

In turn, high speed convection causes jet collimation. The inflow and outflow have nearly equal θ-extents in the case of low-velocity convection (figure 2*b*). As the velocity increases, the entrainment effect causes self-focusing of the outflow while the inflow extent expands and eventually occupies nearly the entire flow domain (figure 7). (Note that narrow jet-like outflows and wide inflows are typical of point-source motion.) This effect is especially strong for ascending convection where the outflow is localized near the axis (while in the descending convection, the outflow is spread over the entire disk). The near-axis outflow must be intense to balance the inflow rate.

Figure 4 illustrates the jet development as Pr decreases from 1 to 0 (see the numbers near the curves) for the no-slip disk. To combine the numerical results for small, large, positive and negative Re in one figure, we have used the rescaled Reynolds number, $Re^* = Re/[1 + |Re|/\log(1 + |Re|)]$, for the ordinate in figure 4(*a*);

note that $Re^* = 0.3Re$ for $|Re| \ll 1$ and $Re^* \approx \mathrm{sign}(Re)\log|Re|$ for $|Re| \gg 1$ (compare the values of Re^* with Re, both of which are shown in figure 4a).

As Pr decreases, no dramatic change occurs in the descending flow (the $Re^* < 0$ branch in figure 4a). In contrast, the ascending flow (the $Re^* > 0$ branch) varies significantly. To show how the flow pattern changes with Pr, figure 4(b), presents profiles of stream function ψ at the fold points of figure 4(a). Recall that $v_r = v(r\sin\theta)^{-1}\,\mathrm{d}\psi/\mathrm{d}\theta$; therefore, the locations of the ψ-maximum in figure 4(b) separate the outflow ($\mathrm{d}\psi/\mathrm{d}\theta > 0$) and inflow ($\mathrm{d}\psi/\mathrm{d}\theta < 0$) regions. As Pr decreases, the location of the maximum moves toward the axis ($\theta = 0$), i.e. the inflow occupies nearly the entire flow region. In the inflow region, v_r (at a fixed r) is bounded as $Pr \to 0$. Since the outflow region reduces to the near-axis boundary layer whose θ-thickness vanishes, v_r increases, i.e. a strong jet develops whose maximum velocity (Re) tends to infinity as $Pr \to 0$.

For large Re, asymptotic analysis is used to obtain explicit relations between Re, Pr and Ra, as detailed below.

6.2. *Asymptotic solution for the near-axis jet*

Consider the boundary layer solution, describing the near-axis jet. Suppose that condition (11d) remains valid in the limit $Re \to \infty$. Then introducing boundary layer coordinate $\eta \equiv Re(1-x)(\approx Re\theta^2/2)$ and allowing $Re \to \infty$ for a fixed η transform (11b) to $\eta\,\mathrm{d}\psi/\mathrm{d}\eta = \psi(1-\psi/4)$, whose solution, satisfying the condition $\psi = 0$ at $\eta = 0$, is

$$\psi = \psi_\mathrm{i} = 4\eta/(4+\eta), \tag{15a}$$

where the subscript i denotes the *inner* solution. (Note that (15a) coincides with the round-jet solution by Schlichting 1933.)

As $\eta \to \infty$, $\psi_\mathrm{i} \to 4$ according to (15a), and therefore, the *outer* solution, $\psi_\mathrm{o}(x)$, must satisfy the condition $\psi_\mathrm{o} = 4$ at $x = 1$, in accordance with the theory of matched asymptotic expansions (Van Dyke 1964). The outer solution, ψ_o is discussed below.

6.3. *Minimum Ra for convection to occur*

In addition to ψ_o, we calculate the limiting value of Ra as $Re \to \infty$ along the $Pr = 0$ curve in figure 4(a). At $Pr = 0$, (11a) reduces to

$$F''' = Ra\psi/(1-x^2).$$

Substituting $\psi = \psi_\mathrm{o}$ yields the equation for the outer solution F_o:

$$F_\mathrm{o}''' = Ra\psi_\mathrm{o}/(1-x^2).$$

The boundary conditions for F_o are the same as those for F:

$$F_\mathrm{o}(0) = F_\mathrm{o}(1) = F_\mathrm{o}'(1) = 0. \tag{15b}$$

Since $\psi_\mathrm{o}(1) \neq 0$, F_o''' has a pole and F_o'' has a logarithmic singularity at $x = 1$. To avoid these singularities in numerical calculations, we decompose F_o into singular and regular parts: $F_\mathrm{o} = F_\mathrm{s} + F_\mathrm{r}$. Let F_s satisfy (15b) and the equation $F_\mathrm{s}''' = Ra4x/(1-x^2)$. Then integration yields

$$F_\mathrm{s} = Ra[2x(\ln 4 - 1 + x) - (1-x)^2\ln(1-x) - (1+x)^2\ln(1+x)].$$

Now, the regular part, F_r must satisfy the equation,

$$F_\mathrm{r}''' = Ra(\psi_\mathrm{o} - 4x)/(1-x^2), \tag{15c}$$

and also the conditions (15*b*). Differentiating (11*b*) and using $\psi_o(1) = 4$ and $F_o'(1) = 0$, we find that $\psi_o(1) = 2$. Then resolving the 0/0 indeterminacy in (15*c*) at $x = 1$ yields $F_r'''(1) = Ra$; thus F_r''' is bounded (while F_s''' is infinite) at $x = 1$.

To calculate ψ_o we apply (11*b*) in the form

$$(1 - x^2)\psi_o' + 2x\psi_o^{-1/2}\psi_o^2 = F_s + F_r. \tag{15d}$$

Equations (15*c*) and (15*d*) are integrated from $x = 1$ to $x = 0$ with initial values $F_r(1) = F_r'(1) = 0$, $\psi_o(1) = 4$. The values of $F_r''(1)$ and of Ra must be adjusted (by shooting) to satisfy the conditions $\psi_o(0) = 0$ and $F_r(0) = 0$. This procedure results in $F_r''(1) = 1.033$ and $Ra = Ra_{\min} = 28.92$. The solid curve for $Pr = 0$ shows ψ_o found numerically and the broken curve P represents the polynomial approximation, $10x^2 - 6x^3$, for ψ_o in figure 4(*b*). The $Pr = 0$ and P curves are indeed very close. Therefore, the multiplicative composite solution, $\psi_a = \psi_o\psi_i/\psi_i(\infty)$, which provides a uniform asymptotic approximation (Van Dyke 1964) for ψ as $Re \to \infty$, can be written in the form

$$\psi_a = (10x^2 - 6x^3)Re(1 - x)/[4 + Re(1 - x)].$$

This formula describes the flow corresponding to the $Pr = 0$ curve in figure 4(*a*) for large Re. To describe high-speed flows for $Pr \neq 0$, we need to consider the temperature field as well.

6.4. *Temperature distribution in the near-axis jet*

Substituting $\eta \equiv Re(1 - x)$ and $\psi = \psi_i$ and allowing $Re \to \infty$ for a fixed η, we transform (9*b*) to the equation

$$2\eta\, \mathrm{d}\vartheta/\mathrm{d}\eta = -\psi_i(1 + Pr\vartheta).$$

Its integration, after use of (15*a*) and (10*b*), yields the following inner solution for $\vartheta t \equiv 1 + Pr\vartheta$:

$$\vartheta t_i = \tfrac{1}{4}(1/Pr + 2)(1 + \eta/4)^{-2Pr}. \tag{16}$$

(Note that (16) coincides with the (large-Re) solution of Rumer 1952.) Since ϑt_i tends to zero as $\eta \to \infty$, the matching condition for the outer solution is $\vartheta t_o(1) = 0$; then (9*b*) yields $\vartheta t_o \equiv 0$. Thus, the near-axis jet transports all heat from the point source and, therefore, (16) is a uniform approximation for the temperature over the entire flow region.

6.5. *Relation among Re, Ra and Pr for high-speed jets*

Using (16), we obtain the outer solution F_o for $Pr \neq 0$ which differs from the solution F_o at $Pr = 0$ (§ 6.3) as discussed below. To find F_o, we need to consider the inner solution F_i.

It is helpful to rewrite (11*a*) using (9*b*) as $F''' = Ra\vartheta'$ and then as $Re^2\mathrm{d}^3F/\mathrm{d}\eta^3 = Ra\,\mathrm{d}\vartheta/\mathrm{d}\eta$. Applying (16) for ϑ, integrating three times, and satisfying (11*c*, *d*) (in the form $F_i(0) = \mathrm{d}F_i/\mathrm{d}\eta(0) = 0$), we obtain the inner solution

$$F_i = [2(1 + \eta/4)^{2-2Pr} - \eta(1 - Pr) - 2]Re^{-2}Raf_{Pr} - C(1 - x)^2, \tag{17a}$$

where C is an integration constant and

$$f_{Pr} = (1 + 2Pr)[Pr^2(1 - Pr)(1 - 2Pr)]^{-1}. \tag{17b}$$

To match the inner (F_i) and outer (F_o) solutions, F_i must be bounded as $Re \to \infty$, and $F_o(x)$ must have, near $x = 1$, the same character as $F_i(\eta)$ for $\eta \gg 1$ (i.e. near the

outer boundary of the jet). According to (17a), this character is different for $Pr < 1/2$ and for $Pr > 1/2$.

If $Pr > 1/2$, the second term dominates the other terms in the square brackets of (17a) as $\eta \to \infty$. Then, neglecting the other terms and requiring (for F_i to be bounded) that

$$Re^{-1}Ra(1+2Pr)[Pr^2(2Pr-1)]^{-1} \to C_1 \quad \text{as} \quad Re \to \infty,$$

we obtain $F_o(x) = C_1(1-x) - C(1-x)^2$. Next, the condition $F_o(0) = 0$ yields $C_1 = C$ and, therefore, $F_o = Cx(1-x)$. Note that at $x = 1$, F_o'' is regular for $Pr > 1/2$ in contrast to the singular F_o'' at $Pr = 0$. To obtain the outer solution $\psi_o(x)$, we substitute $F = F_o$ in (11b), as follows:

$$(1-x^2)\psi_o' + 2x\psi_o - \tfrac{1}{2}\psi_o^2 = Cx(1-x).$$

Integrating and satisfying the conditions, $\psi_o(0) = 0$ and $\psi_o(1) = 4$, we find $C = 15.29$. (This solution coincides with that found by Schneider 1981 for a jet emerging from a hole in a no-slip plane.) Thus, we obtain the asymptote (e.g. for the $Pr = 1$ curve in figure 4a),

$$Re = Ra(1+2Pr)[CPr^2(2Pr-1)]^{-1} \quad \text{for} \quad Re \gg 1 \quad \text{and} \quad Pr > 1/2.$$

If $Pr < 1/2$, the first term in the square brackets of (17a) dominates the other terms as $\eta \to \infty$. Then, neglecting the other terms and requiring (for F_i to be bounded) that

$$2^{4Pr-3} f_{Pr} Re^{-2Pr} Ra \to C_1 \quad \text{as} \quad Re \to \infty,$$

we obtain $F_o(x) = C_1(1-x)^{2-2Pr} - C(1-x)^2$. Again, the condition $F_o(0) = 0$ yields $C_1 = C$ and, therefore, $F_o = C[(1-x)^{2-2Pr} - (1-x)^2]$. (Note two important features: (i) the F_o solutions for $Pr > 1/2$ and $Pr < 1/2$ coincide at $Pr = 1/2$, and (ii) for $0 < Pr < 1/2$, F_o'' has a power-law singularity, $F_o'' \sim (1-x)^{-2Pr}$ as $x \to 1$, while for $Pr = 0$, F_o'' has a logarithmic singularity at $x = 1$.) To find the outer solution ψ_o we apply $F_o(x)$ to (11b):

$$(1-x^2)\psi_o' + 2x\psi_o - \tfrac{1}{2}\psi_o^2 = C[(1-x)^{2-2Pr} - (1-x)^2]. \tag{17c}$$

Integrating (17c) from $x = 1$ to $x = 0$ with the condition, $\psi_o(1) = 4$, and satisfying the condition $\psi_o(0) = 0$, we determine C as a function of Pr. Therefore, we obtain the asymptote (e.g. for the $Pr = 0.3$ curve in figure 4a),

$$Ra = Re^{2Pr} C(Pr) 2^{3-4Pr} / f_{Pr} \quad \text{for} \quad Re \gg 1 \quad \text{and} \quad Pr < 1/2. \tag{17d}$$

For $Pr \ll 1$ (the case relevant for high-speed jets), (17b) yields $f_{Pr} = Pr^{-2}$, and the asymptote for $C(Pr)$ is $C_a = (2Pr)^{-1}$. The latter relation follows from the requirement that the F_o'' singularity at $x = 1$ transforms from a power-law to a logarithmic type as $Pr \to 0$, i.e. the right-hand side of (17c) must produce the term $-(1-x)^2 \ln(1-x)$ as $Pr \to 0$ (see the expression for F_s in § 6.3).

Using $f_{Pr} = Pr^{-2}$ and $C = (2Pr)^{-1}$ we reduce (17d) to

$$Ra = 4PrRe^{2Pr} \quad \text{for} \quad Re \gg 1 \quad \text{and} \quad Pr \ll 1 \tag{17e}$$

(e.g. for the $Pr = 0.1$ curve in figure 4a). Substituting $Ra = Ra_F$ and $Re = Re_F$ in (17e) yields the asymptote, $Re_F = (\frac{1}{4}Ra_F/Pr)^{1/(2Pr)}$, for the fold points in figure 4(a) as $Pr \to 0$.

Thus, the buoyancy force generates a high-speed collimated jet for small Pr because (i) negative 'feedback' of convection is weak and (ii) the entrainment effect causes self-focusing of the outflow. In contrast, swirl imposed on the disk decreases the jet

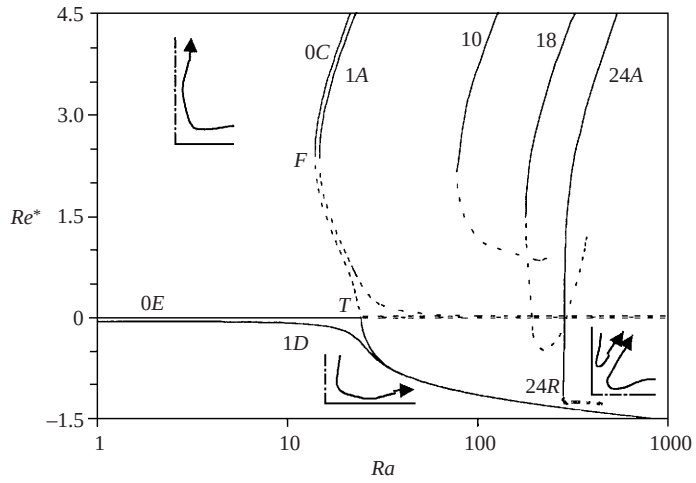

FIGURE 5. Convection above the swirling disk. Numbers near the curve indicate the values of the swirl Reynolds number Re_s. Letters next to the numbers denote the equilibrium state (E), the swirl-free convection (C), and the swirling ascending (A), descending (D), and reversed-near-the-axis (R) flows. Insets show the flow patterns for ascending ($Re^* > 0$), descending, and reversed-near-the-axis flows. $Pr = 0.1$.

velocity. Since the centrifugal force is directed away from the axis of rotation, it widens the near-axis jet by pushing the fluid toward the periphery. Moreover, swirl can make this jet annular, and can even reverse the flow near the axis.

7. Effects of swirl on the jets

7.1. *Breakdown of the transcritical bifurcation*

To study swirl effects, we consider a potential-vortex flow imposed on the disk. In this case,

$$v_\phi = \nu(r\sin\theta)^{-1}\Gamma(x), \tag{18a}$$

where Γ is the velocity circulation along a circle $\{r = \text{const}, \theta = \text{const}\}$ divided by $2\pi\nu$. With the help of (18a), (8) (except for v_ϕ), and (2) we obtain the equation for Γ:

$$(1-x^2)\Gamma'' = \psi\Gamma'. \tag{18b}$$

The boundary conditions for Γ are

$$\Gamma(1) = 0 \quad \text{and} \quad \Gamma(0) = Re_s. \tag{18c}$$

Here the swirl Reynolds number Re_s is the circulation on the disk divided by $2\pi\nu$. The integration of (18b) starts from $x = 1$ with $\Gamma(1) = 0$ and a guessed value of $\Gamma'(1)$. Then we adjust $\Gamma'(1)$ by shooting to satisfy $\Gamma(0) = Re_s$. Finally, for swirling flows, (11a) is modified to

$$(1-x^2)F'''' = Ra\psi(1 + Pr\vartheta) + 2\Gamma\Gamma'. \tag{18d}$$

Figure 5 shows the results for the swirling disk (with the symmetry condition for ψ) at $Pr = 0.1$. Numbers near the curves indicate the Re_s values while the letters denote the flow state: E the equilibrium state, C the swirl-free convection, A ascending, D descending, and R reversed-near-the-axis swirling flows. Solid curves represent stable flow states, and broken curves represent unstable solutions.

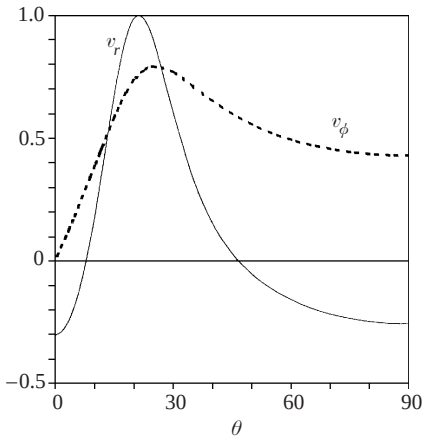

FIGURE 6. Velocity profiles for the two-cell swirling flow at the fold point on curve 24R in figure 5.

The swirl destroys the transcritical bifurcation T: ascending (curve 1A) and descending (curve 1D) modes are separated at $Re_s = 1$, unlike curves 0C and 0E at $Re_s = 0$ in figure 5. The fold bifurcation F survives for $Re_s \neq 0$ and again allows the appearance of bipolar jets through a fold catastrophe as Ra increases. For the stable outflows (solid branches for $Re > 0$), the maximum velocity (Re) is smaller for swirling flows than that for swirl-free convection at the same Ra.

7.2. *Development of conical jets*

As Re_s increases, the fold point F (separating the stable and unstable solution branches) moves to the right and downward and eventually crosses the line $Re = 0$ (curves 10, 18, and 24 in figure 5). The crossing corresponds to the flow reversal near the axis. First, such a reversal occurs for the unstable lower branch (curve 18 for $Re < 0$), and then for the stable upper branch as well (curve 24R). Curve 24 comprises the branches 24A (ascending flow) and 24R (reversed-near-the axis flow, see the inset near curve 24R).

Figure 6 shows profiles of the radial (v_r) and azimuthal (v_ϕ) velocities (both normalized by the maximum of v_r) at the fold point of curve 24R in figure 5. There are two inflow ($v_r < 0$) regions in figure 6: $\theta < 10^\circ$ and $\theta > 35^\circ$, and an annular conical outflow ($v_r > 0$) in between. Our calculations show that flow reversal near the axis occurs when the ratio of the maximum swirl velocity to the maximum radial velocity exceeds 0.7 (a value typical of vortex breakdown, e.g. see Shtern & Hussain 2000).

7.3. *High-speed swirling jet*

Even for large Re_s, the jet remains consolidated as long as buoyancy (which pushes the flow along the axis) dominates the centrifugal effect (which pushes the jet away from the axis), e.g. see curve 24A in figure 5 for large Re. To describe these weakly swirling high-speed jets, the asymptotic analysis of § 6 must be generalized to include the swirl.

For large Re, the solution for circulation Γ has two parts: for a near-axis boundary layer and for an inviscid outer flow. In the outer flow, the linear (viscous) term on the left-hand side of (18b) is negligible, and therefore $\Gamma' = 0$, i.e. circulation is constant: $\Gamma \equiv Re_s$ for $0 \leqslant x < 1$. Within the boundary layer, the circulation drops

to zero on the axis. Using the inner variable $\eta = Re(1-x)$ and (15a), we reduce (18b) to $\mathrm{d}^2\Gamma/\mathrm{d}\eta^2 = 2(4+\eta)^{-1}\,\mathrm{d}\Gamma/\mathrm{d}\eta$. Integrating and using the conditions $\Gamma = 0$ at $\eta = 0$ and $\Gamma \to Re_s$ as $\eta \to \infty$, yields $\Gamma = Re_s\eta/(4+\eta)$. This solution is a uniform approximation for Γ over the entire flow region as well.

Now, we consider how the swirl modifies the ascending meridional flow. We show (below) that the outer solution ψ_o increases with Ra in swirling convection (unlike the constraint that $\psi_\mathrm{o} < 4$ in the swirl-free case, figure 4b). Then for large Ra, the linear terms on the left-hand side of (11b) become negligible, yielding $\psi_\mathrm{o} = (-2F_\mathrm{o})^{1/2}$. Substituting $F = F_\mathrm{o} = -2Ra^2W$ and $\psi = \psi_\mathrm{o} = 2RaW^{1/2}$ in (18d), putting $Pr = 0$ and $\Gamma' = 0$, and using the conditions $\psi_\mathrm{o}(0) = \psi_\mathrm{o}(1) = 0$, we obtain

$$(1-x^2)W''' = -W^{1/2}, \quad W(0) = W'(0) = W(1) = 0. \tag{19}$$

In addition to $W \equiv 0$, the problem (19) has a non-trivial solution where $W''(0) = 0.00478$ (giving the radial velocity on the disk, $v_r(0) = -Ra[2W''(0)]^{1/2}\nu r^{-1}$) and $W'(1) = -0.00606$ (used below).

The outer solution, $\psi_\mathrm{o} = 2RaW^{1/2}$, resulting from (19) does not match the inner solution ψ_i: $\psi_\mathrm{o}(1) = 0$ where $\psi_\mathrm{i} = 4$ as $\eta \to \infty$ according to (15a). Therefore, an intermediate boundary layer exists between the near-axis jet and the outer flow. The solution ψ_io for this intermediate boundary layer must satisfy the equation

$$\xi\mathrm{d}\psi_\mathrm{io}\mathrm{d}\xi = \psi_\mathrm{io} - \psi_\mathrm{io}^2/4 + 2\xi, \quad \xi = (1-x)Re_s^2/8. \tag{20a}$$

We have deduced (20a) from (11b) using $F = -(1-x)Re_s^2/2$. (This approximation for F near the axis follows from the solution by Long 1961 for swirling jets.) Matching ψ_io and ψ_i yields the condition $\psi_\mathrm{io} = 4$ at $\xi = 0$. Since $\psi_\mathrm{io} \to Re_s(1-x)^{1/2}$ as $\xi \to \infty$ and $\psi_\mathrm{o} = 2Ra|W(1)|^{1/2}(1-x)^{1/2} + O(1-x)$ near $x = 1$, matching ψ_io and ψ_o yields the asymptotic relation

$$Re_s = 2|W'(1)|^{1/2}Ra. \tag{20b}$$

This relation, when applied to obtain the value of Ra at the collapse point as a function of Re_s, agrees well with the numerical results for large Re_s. Thus, (20b) explains the shift of the curves in figure 5 to the right as Re_s increases. Note that the large-Re slopes of these curves, being determined by (17e), do not depend on Re_s. Using (20b) and (17e), we can estimate the angular thickness of both the boundary layers in terms of Ra : $\theta_\mathrm{i} \sim O(Ra^{-1/(4Pr)})$ for ψ_i and $\theta_\mathrm{io} \sim O(Ra^{-1})$ for ψ_io (figure 7). As θ increases in the tail region, $\theta_\mathrm{i} < \theta < \theta_\mathrm{io}$, the jet velocity decreases slower, $v_r \sim \theta^{-1}$ (the dashed curve in figure 7), than the Schlichting jet ($v_r \sim \theta^{-4}$, the solid curve). The Schlichting jet (15a) approximates the solution in the core region $0 < \theta < \theta_\mathrm{i}$ well. Such a core–tail structure is typical of weakly swirling jets (Shtern & Hussain 2000).

Now we show that the ascending convection with high-speed jets is stable.

8. Stability of conical buoyancy-driven flows

8.1. *Problem of spatial linear stability*

First, we study the spatial linear stability of the convection flows and then the weakly unsteady and weakly nonlinear dynamics of disturbances that result in switching between the steady states (e.g. see arrows *FE* and *TC* in figure 3). For conical convection (considered here as the base flow), $\boldsymbol{u} \equiv r\boldsymbol{v}$ and $\vartheta \equiv r(T - T_\infty)/(\gamma Pr)$ depend only on θ. Therefore, the equations for infinitesimal steady disturbances of $\boldsymbol{u}$ and ϑ allow normal-mode (exponential) solutions with respect to $\ln r$ and ϕ, e.g.

$$\vartheta = \vartheta_b(\theta) + A\vartheta_d(\theta)r^\alpha\cos(m\phi). \tag{21}$$

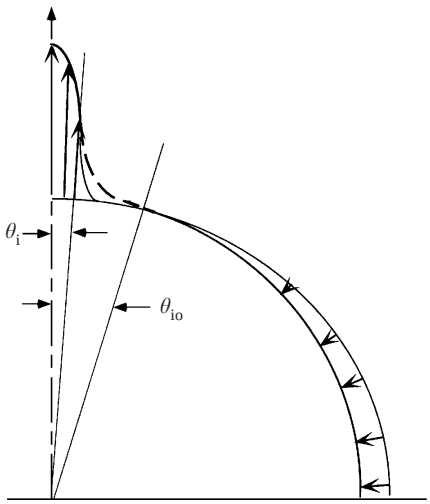

FIGURE 7. Schematic (not to scale) of $v_r(\theta)$ (radial arrows) at fixed r for large-Re swirling flows in figure 5. The near-axis jet has the Schlichting-jet core, $\theta < \theta_{\rm i} \sim Ra^{-1/(4Pr)}$, and the tail, $\theta_{\rm i} < \theta < \theta_{\rm io} \sim Ra^{-1}$, where v_r decays slower (dashed line) than in the Schlichting jet (solid line).

The indices b and d denote the base state and the disturbance, the amplitude A is some constant, and m is some prescribed integer (the azimuthal wavenumber). The velocity and pressure disturbances have similar representations. The exponent α is the unknown eigenvalue. Thus, the stability problem exactly reduces to ordinary differential equations (e.g. for ϑ_d) despite the strongly non-parallel nature of the base flow (figure 2b). We omit here the details of this reduction and present only the results since the algebra is cumbersome but straightforward and quite similar to that for swirl-free (Shtern & Hussain 1998) and swirling (Shtern & Drazin 2000) conical flows. The new elements are the temperature equation and the buoyancy-force term in the radial momentum equation; both these elements can be included without any difficulty.

The exponent α characterizes the spatial stability. Since a point–source solution is a far-field approximation, we consider the behaviour of the disturbance as $r \to \infty$. If $\alpha < 0$, the disturbance decays faster than the base flow; if $\alpha = 0$, the disturbances and base flow have the same r-dependence; and if $\alpha > 0$, the ratio of the disturbance to the base flow amplitude increases with r. Accordingly, $\alpha < 0, \alpha = 0$, and $\alpha > 0$ correspond to stability, neutral stability, and instability of the base flow.

8.2. *Instability causing hysteretic transitions*

Figure 8 shows the results for the problem with the stress-free condition on the disk at $Pr = 1$ and $Re_s = 0$. The curve $ACFTD$ and the $Re = 0$ line represent the base flow and the rest state (as in figure 3a). Curves α_E and α_C show the scaled spatial stability growth rate ($10 \times \alpha$); α is a real number in this case. Subscripts E and C indicate the equilibrium (rest) state and convection. Curve α_E represents the analytical solution (4) at $l = 2$ and shows that the rest state is stable, $\alpha_E < 0$, for $Ra < 24$ and unstable, $\alpha_E > 0$, for $Ra > 24$.

Curve α_C depicts the numerical results for the stability of the convective flow ($ACFTD$) with respect to axisymmetric ($m = 0$) disturbances. In the vicinity of the bifurcation point T, α_E has the opposite sign to that of α_C, i.e. the principle of

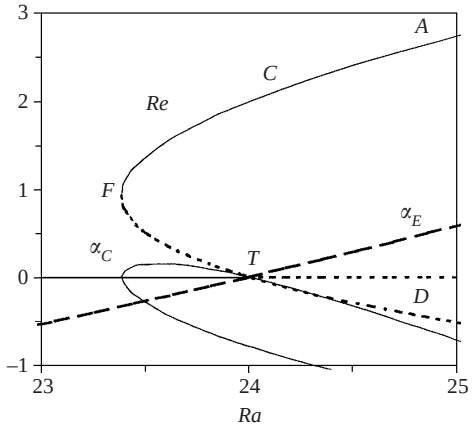

FIGURE 8. Spatial stability growth rate ($10 \times \alpha$) for the equilibrium state (curve α_E) and for convection (curve α_C) vs. Rayleigh number Ra. Curve $ACFTD$ shows $Re(Ra)$ for the basic flow near the swirl-free symmetry disk at $Pr = 1$ (as in figure 3*a*). The lower branch α_C corresponds to stable convection (branch ACF).

exchange of stabilities is valid: the flow is stable when the rest state is unstable and vice versa.

The most interesting result is that the flow becomes stable for the solution branch FCA in figure 8. When one moves away from T along curve TF, curve α_C shows that α first increases, reaches its maximum value of $\alpha = 0.0154$ at $Ra = 23.56$, then decreases, and crosses zero at the fold point F. The fact that α changes its sign exactly at F serves as a check for the numerical calculations. The lower branch of curve α_C corresponds to the upper branch FCA. Since $\alpha < 0$ on the lower branch of curve α_C, the flow is stable along FCA.

Similar changes in stability at fold point-occur in the flow with the no-slip (as well as the swirling) disk. In the no-slip case, there is no three-dimensional instability of the descending flow near the bifurcation point T (figure 3*b*). In the next section, we develop the weakly nonlinear approach for the hysteretic transitions between the states.

8.3. *Amplitude equations for spatiotemporal disturbances*

To investigate the spatiotemporal nonlinear dynamics of transient trajectories, we deduce amplitude equations of the Ginzburg–Landau type with the help of the expansion

$$\vartheta = \vartheta_{b0} + \varepsilon\vartheta_{b1} + \varepsilon A(\varepsilon\tau, \xi)\vartheta_{d1}(x) + \varepsilon^2 A_2(\varepsilon\tau, \xi)\vartheta_{d2}(x) + \cdots \tag{22}$$

(and similar expansions for the velocity and the pressure). Here $\varepsilon \equiv Ra - Ra_F$ is the small parameter and amplitude A is of $O(1)$ in the vicinity of the fold point F. Indices b and d denote the base flow and the disturbance respectively; subscripts 0, 1 and 2 correspond to the powers of ε; $\tau = \nu t/r_0^2$ and $\xi = \ln(r/r_0)$ where r_0 is an arbitrary value of r within the region of conical similarity.

Expansion (22) involves only axisymmetric ($m = 0$) disturbances because we consider the transition between the axisymmetric flow states. Upon substitution of (22) in (2), the resulting terms of $O(1)$ constitute the equations for the base flow at $Ra = Ra_F$, and terms of $O(\varepsilon)$ constitute the linear stability equations and also describe the variation of the basic flow as Ra changes (ϑ_{b1}). The solvability condition for terms of

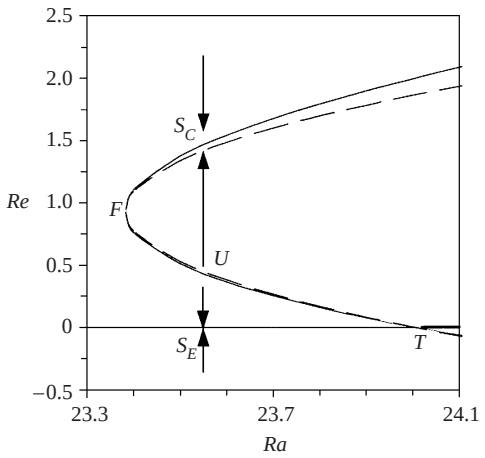

FIGURE 9. Weakly nonlinear approximation (broken curve) for steady swirl-free convection (solid curve) and transient trajectories (arrows) described by the amplitude equation (24). $Pr = 1$.

$O(\varepsilon^2)$ results in the amplitude equation

$$A_s = \exp(-2\xi)[\gamma A - \delta A^2 + (A_{\xi\xi} - \beta A_\xi)/\varepsilon], \tag{23}$$

where $s = \varepsilon\tau$ is the 'slow' time, and the subscripts denote differentiation. Values of the coefficients β, γ and δ follow from the expansion. We omit the detailed derivation of (23) because it is similar to that in Shtern & Hussain (1998) and Shtern & Drazin (2000). Moreover, (23) coincides with the amplitude equation obtained in Shtern & Hussain (1998) for a fold point in conical solutions of the Navier–Stokes equations.

All terms in (23) are of $O(1)$ since A_ξ and $A_{\xi\xi}$ are both of $O(\varepsilon)$. For a finite region $\xi_i \leqslant \xi \leqslant \xi_o$ we use the boundary conditions $A_\xi(\xi_i) = A_\xi(\xi_o) = 0$ which are consistent with the conical similarity of the base flow. There are two steady ξ-independent solutions of (23): $A = 0$, corresponding to the unstable branch FT in figure 3(a), and $A = \gamma/\delta$, corresponding to the branch FC. Equation (23) governs the transition from the unstable to stable branches at $Ra = Ra_F + \varepsilon$ (e.g. from U to S_C in figure 9) and also the evolution of the disturbance shown by the upper arrow in figure 9. Equation (23) does not describe the transition from U to S_E in figure 9. Along line $US_E, |A|$ becomes infinite at a finite time according to (23) – a limitation typical of a weakly nonlinear approach.

To overcome this drawback and to involve all three steady ξ-independent solutions in the range $Ra_F < Ra < Ra_{cr}$, (e.g. the stable convection, S_C, the unstable convection, U, and the stable rest state, S_E, in figure 9), we modify (23) by adding a term proportional to A^3. Also, we change the reference value and the normalization to make $A = 0$ at the rest state and $A = Re$ for the steady-flows. Then (23) transforms into the equation

$$A_s = \exp(-2\xi)\{\gamma A[\sigma - (A - Re_F)^2] + (A_{\xi\xi} - \beta A_\xi)/\varepsilon\}, \tag{24}$$

where $\sigma = Re_F^2(Ra - Ra_F)/Ra_{cr} - Ra_F)$ (we recall that subscript F indicates values at the fold F). The broken curve in figure 9, depicting $(Re - Re_F)^2 = \sigma$, passes through F and T, approximates the unstable branch FUT well, and approximates the stable branch FS_C satisfactorily. In (24), β and $\gamma(\sigma - Re_F^2)$ are spatial and temporal growth rates of the infinitesimal disturbances of the rest state. Since this state is linearly

stable for $Ra < Ra_{cr}$, $\beta < 0$ and $\gamma(\sigma - Re_{af}^2) < 0$ in this range. Equation (24) describes transient trajectories (arrows in figure 9) near the stable (e.g. S_E and S_C) and unstable (e.g. U) steady states, and therefore hysteretic transitions between the rest state and ascending convection (figure 3*a*). Equation (24) governs hysteretic transitions for the no-slip disk as well (figure 3*b*). Thus, the strong jets corresponding to ascending convection (e.g. the upper branches in figures 3 and 5) are stable near the fold points (at least).

9. Concluding remarks

The primary objective of this paper is to demonstrate that buoyancy can generate strongly collimated bipolar jets evolving from the spherically symmetric rest state near a point source of heat and gravity. To this end, we have considered a simple problem described by conically similar solutions of the Boussinesq equations. The problem symmetry permits detailed parametric, asymptotic, stability, and bifurcation analyses, and even analytical solutions, which reveal a number of interesting effects: convection onset via instability and bifurcation, jet collimation, flow reversal near the axis (due to swirl imposed on the accretion disk), and hysteretic transitions between the steady states.

An important element of our approach is the modelling of the accretion disk as an infinite impermeable equatorial plane. This causes flow symmetry with respect to the disk, and in particular, the bipolar character of jets. We have considered (*a*) no-stress, (*b*) no-slip, and (*c*) potential-swirl conditions on the disk. The no-slip condition does not affect the flow outside the near-disk boundary layer for high-speed jets ($Re \gg 1$) but affects the stability and bifurcation features of low-speed convection. On the other hand, the symmetry condition (due to its inviscid nature) remains important over the entire flow domain and affects both low-speed and high-speed convection.

The simplicity of the model allows us to analytically solve the problem of the rest-state instability (§ 3) and to obtain analytical solutions for the nonlinear problem of bifurcation of thermal convection (§ 4). As Ra exceeds its critical value Ra_{cr}, two stable states of steady convection appear for the no-slip disk (figure 3*b*): (i) the ascending flow (A) which consists of an outflow normal to the disk and a radial inflow along the disk, and (ii) the descending flow (D) which has the opposite direction to that of A.

The velocity of flow D gradually increases from zero as Ra increases beyond Ra_{cr}. In contrast, stable flow A can only exist at high speeds; its maximum velocity (Re) is substantially larger than that for D (at the same values of Ra and r). As Ra increases, flow A develops via saturation of finite-amplitude disturbances (of the rest state or of flow D) and disappears via a fold catastrophe as decreasing Ra reaches $Ra_F < Ra_{cr}$ (e.g. at F in figure 3). Thus, the model predicts that the bipolar outflows appear and disappear via hysteretic transitions (§ 5).

The high-speed character of flow A becomes more prominent as the Prandtl number Pr decreases, since the negative 'feedback' (advection-induced change in the temperature field) weakens. Indeed, the velocity on the axis (Re) tends to infinity for finite Ra as $Pr \to 0$ (figure 4*a*); accordingly, the angular width of the outflow tends to zero. Hence buoyancy-generated high-speed collimated jets arise. We have developed an asymptotic approach for $Re \gg 1$ and have obtained analytical solutions describing the near-axis jet and the entrained flow (§ 6).

We have extended the problem to the case of a potential-vortex motion of the disk material (to mimic cosmic flows). The swirl destroys the transcritical bifurcation T (figure 5), and thus separates the solution branches corresponding to ascending

(A) and descending (D) convection. However, the swirl retains the fold bifurcation (at $Ra = Ra_F$), allowing hysteretic appearance and disappearance of high-speed jets (figure 5). As the disk circulation (Re_s) becomes large, it gives rise to new important effects (§ 7): (i) Ra_F increases proportionally to Re_s, (ii) the near-axis jet transforms into a conical annular jet, and (iii) flow reversal occurs near the axis (figure 6).

Such a detailed parametric study is possible due to the similarity that allows us to reduce the Boussinesq equations to ordinary differential equations. The similarity also allows us to develop an efficient stability analysis technique for these strongly non-parallel flows (§ 8), and to study (i) the linear instabilities with respect to time-independent disturbances leading to hysteretic transitions (figure 8), and (ii) the spatiotemporal nonlinear dynamics of the disturbances near the steady states (equation (24) and figure 9).

This technically simple problem has a number of features analogous to those of geophysical and astrophysical flows. The point-source model is the limiting case for thermal convection between spherical shells. Shell convection has been extensively studied for modelling large-scale circulation in planets and stars (Chandrasekhar 1981; Busse 1975), and for the mathematical aspects related to bifurcation in spherically symmetric systems (Chossat 1979; Golubitsky & Schaeffer 1982). In the limiting case of a narrow shell, the problem reduces to a horizontal layer heated from below, for which Rayleigh (1916) obtained the first analytical solution of convection. Surprisingly, the other limiting case where the outer to inner radius ratio tends to infinity (and gravity is due to the mass of the inner sphere only) has not so far been studied. As in the Rayleigh problem, the point-source limiting case also permits analytical solutions obtained here.

Interestingly, buoyancy jets have some similarity with astrophysical outflows. These outflows emerge from young stars, double stars, dying stars, and galaxy cores (whose masses range from 0.01 to 10^9 of the mass of the Sun), have sizes of 0.1–10^6 parsecs (1 parsec $\approx 3 \times 10^{13}$ km), and have velocities ranging from tens of km s^{-1} to relativistic ones (Bachiller 1996; Ferrari 1998; Pudritz 2000). The fact that the appearance of jets seems to be a generic phenomenon – occurring in such a variety of objects and scales – motivated us to investigate whether a simple fluid-mechanics model can demonstrate the development of strongly collimated outflows.

Our model differs from the very complex astrophysical jets in many aspects: (a) the density gradients are due to the temperature gradients in our case, but not so in cosmic jets; (b) rotation is potential here, while it is Keplerian in cosmic accretion disks; (c) the Boussinesq approximation we use is not valid for astrophysical applications; (d) velocity and temperature fields are conically similar in our problem, but they are not so in cosmic jets; (e) the thermal energy of stars and galaxy cores is transported by radiation, and not via diffusion as modelled here; and (f) our study is limited to incompressible flows while cosmic jets are hypersonic and even relativistic.

Nevertheless, the model has a few important features in common with cosmic outflows: gravity and density gradients, and an accretion disk. Our study has shown that these features alone are sufficient for the formation of collimated bipolar jets. Other common features – the concentration of magnetic field and the formation of spiral branches – will be reported separately.

This research received partial support from NSF grants CTS 9622302 and CTS 9904328. F. H. acknowledges support for participation at the 2000 Hydrodynamic Turbulence Program of ITP, UCSB.

REFERENCES

Bachiller, R. 1996 Bipolar molecular outflows from young stars and protostars. *Ann. Rev. Astron. Astrophys.* **34**, 111–154.

Busse, F. H. 1975 Patterns of convection in spherical shells. *J. Fluid Mech.* **72**, 67–85.

Chandrasekhar, S. 1981 *Hydrodynamic and Hydromagnetic Stability*. Dover.

Chossat, P. 1979 Bifurcation and stability of convective flows in a rotating or not rotating spherical shell. *SIAM J. Appl. Maths.* **37**, 624–647.

Ferrari, A. 1998 Modeling extragalactic jets. *Ann. Rev. Astron. Astrophys.* **36**, 539–598.

Golubitsky, M. & Schaeffer, D. 1982 Bifurcation with O(3) symmetry including applications to the Bénard convection. *Commun. Pure Appl. Maths* **35**, 81–111.

Landau, L. D. 1944 On exact solution of the Navier–Stokes equations. *Dokl. Akad. Nauk SSSR* **43**, 299–301.

Long, R. R. 1961 A vortex in an infinite viscous fluid. *J. Fluid Mech.* **11**, 611–623.

Pudritz, R. I. 2000 Jets from accretion discs. *Phil. Trans. R. Soc. Lond.* A **358**, 711–757.

Rayleigh, Lord 1916 On convection currents in a horizontal layer of fluid, when the highest temperature is on the under side. *Phil. Mag.* (6) **32**, 529–546.

Rumer, Yu. B. 1953 Convective diffusion in a submerged jet. *J. Appl. Math. Mech.* **17**, 743–744.

Schlichting, H. 1933 Laminare Strahlausbreitung. *Z. Angew. Math. Mech.* **13**, 260–263.

Schneider, W. 1981 Flow induced by jets and plums. *J. Fluid Mech.* **108**, 55–65.

Shtern, V. & Drazin, P.G. 2000 Instability of a free swirling jet driven by a half-line vortex. *Proc. R. Soc. Lond.* A **456**, 1139–1161.

Shtern, V. & Hussain, F. 1998 Instabilities of conical flows causing steady bifurcations. *J. Fluid Mech.* **366**, 33–85.

Shtern, V. & Hussain, F. 2000 New features of swirling jets. *Phys. Fluids* **12**, 2868–2877.

Van Dyke, M. 1964 *Perturbation Methods in Fluid Mechanics*. Academic.